# Universidad Carlos III de Madrid
## e-Archivo

Institutional Repository

# Wide band energy analysis of fluidized bed pressure fluctuation signals using a frequency division method

Jesús Gómez-Hernández *, Javier Sánchez-Prieto, Javier Villa Briongos, Domingo Santana

*Carlos III University of Madrid (Spain), Energy Systems Engineering Group, Thermal and Fluids Engineering Department, Avda. de la Universidad 30, 28911 Leganés, Madrid, Spain*

**Abstract:** A statistical method based on approximation of the cumulative energy distribution by Student's *t*-distribution is proposed for the unbiased frequency domain division. The proposed method fixes the number of samples needed to estimate the power spectrum and its corresponding cumulative energy distribution using the Kolmogorov–Smirnov test. The reliability of the method to divide the frequency domain was shown for different fluidization velocities by changing the bed aspect ratio and using different pressure probes. Water-induced defluidization tests were conducted to illustrate the use of wide band energy as a monitoring tool. The Student's *t*-distribution results are compared with an analysis performed using the traditional visual inspection method. The energy of the power spectrum contained within the frequency regions obtained by the visual method is not able to detect changes in the bed aspect ratio or the start of the rotating distributor. No meaningful differences could be observed in the frequency regions using different quality pressure sensors because the approach using Student's *t*-distribution focuses on the sharp energy increase produced by the primary frequencies of the power spectrum. The sensitivity exhibited by the proposed frequency division approach for the range of fluidization conditions tested improves the use of the energy contained in these regions as a diagnostic tool in fluidized bed processes.

## 1. Introduction

Pressure fluctuations are one of the most commonly measured parameters used for the monitoring of fluidized beds (van der Schaaf et al., 1998). There are several methods proposed in the literature to analyze such signals, which can be grouped into three categories as a function of the domain type: (1) time, (2) frequency and (3) state space (van Ommen et al., 2011). Focusing on the frequency domain analysis type, it is typically performed using power spectral density (PSD) analysis (Brown and Brue, 2001).

The frequency analysis of pressure fluctuations is used to obtain information about the fluidization dynamics and to diagnose the fluidization state (Kage et al., 2000). Characteristic features of the power spectrum have been used for the description of the fluidization regime. For example, the frequency peak and the dominant frequency have been used to detect defluidization in coating and drying processes (Parise et al., 2011; de Martin et al., 2011). The coherent standard deviation and the average frequency of pressure fluctuations have also been used to estimate the bubble size and to detect the regime transitions in slurry bubble columns (Chilekar et al., 2005; Ruthiya et al., 2005). Similarly, the type of the power spectrum fall-off with frequency has been used as a tool for distinguishing between deterministic and noise systems (Johnsson et al., 2000; van der Schaaf et al., 1999, 2004; van Ommen et al., 2011; Vander Stappen, 1996). Another important parameter obtained

---
\* Corresponding author. Tel.: +34916248371; fax: +34916249430.
*E-mail address:* jegomez@ing.uc3m.es (J. Gómez-Hernández).

from the frequency domain is the energy contained within the power spectrum. According to Johnsson et al. (2000), this variable, the wide band energy, reflects the change in operational regimes and can be used to characterize the structure of a fluidized bed. More recently, the wide band energy has been used to detect defluidization phenomena (Gómez-Hernández et al., 2012).

The use of the wide band energy as a monitoring tool presents some advantages in comparison to other parameters obtained from the frequency domain. The easy and fast computation of the wide band energy provides a reliable view of the dynamic behavior of the system once the power spectrum is properly divided into a set of frequency regions (Briongos and Guardiola, 2003; Gómez-Hernández et al., 2012; van der Schaaf et al., 2002, 2004). Traditionally, this type of frequency division has been conducted using visual selection of the cut-off frequencies between the different spectral regions. In this procedure, the observer visually identifies the frequency limits by studying the behavior of the frequency domain either in the power spectrum (Johnsson et al., 2000; van der Schaaf et al., 1999; Vander Stappen, 1996) or as the cumulative energy distribution (Gómez-Hernández et al., 2012). However, the visual inspection approach has at least two major drawbacks, as follows: (i) the cut-off frequencies obtained through the visual inspection depend on the observer and (ii) the power spectrum fall-off is unavoidably affected by the quality of the measured signal, i.e., the transducer type and the signal conditioning. Consequently, the division of the frequency domain as a function of the power spectra or the cumulative energy distribution is not always a reliable process. Therefore, to conduct a reliable wide band energy computation, it is necessary to remove the bias introduced by the observer.

In this study, a procedure for the systematic computation of the wide band energy is developed. The proposed methodology is based on a Student's $t$-distribution fitting of the power spectrum cumulative energy (CE). The Kolmogorov–Smirnov test is used to compare the cumulative energy with Student's $t$-distribution. As a result, three frequency regions are found. The differences that appear at the distribution tails when comparing the cumulative energy with the corresponding Student's $t$-distribution discriminate the cut-off frequencies that separate the three frequency regions.

## 2. Experimental setup

Two cylindrical lab-scale Bubbling Fluidized Beds (BFBs) were used for the experiments. The first apparatus is a cylindrical poly methyl methacrylate (PMMA) vessel with a 0.07 m inner diameter, $d$, and a 1 m height. The air distributor consists of 7 tuyeres with eight 0.5 mm diameter holes in each. The plenum is filled with a metallic mesh to ensure homogeneous air distribution. The bed aspect ratio is fixed at $h_b/d = 1$.

The second fluidized bed facility (Fig. 1) is equipped with an electric motor to rotate the distributor. The cylindrical vessel has an inner diameter, $D$, of 0.192 m, and a height of 1 m (Soria-Verdugo et al., 2011). The fixed bed height, $h_b$, is fixed at $0.75 \cdot D$. The rotating distributor consists of a perforated plate with 275 orifices of 2 mm diameter each, arranged in a triangular configuration with an 11 mm pitch. There are two types of experiments conducted in this facility, those with the distributor rotating at an angular velocity of 100 rpm and those with a static distributor.

The bed material was silica sand particles for all experiments, classified as Group B according to the Geldart's classification (Geldart, 1973). The particle density was measured at 2645.5 kg/m³ with a standard deviation of 2.5 kg/m³, and a mean diameter of 683 μm. The beds were fluidized with air at ambient conditions, and the airflow was measured with a rotameter. The minimum fluidization velocity was measured at $U_{mf,s} = 0.33$ m/s and $U_{mf,r} = 0.31$ m/s for the static and rotating distributor, respectively (Sobrino et al., 2008).

The measurement system in the small facility ($d = 0.07$ m) consisted of one pressure probe placed at the plenum chamber with 4 mm inner diameter and 0.10 m length. These dimensions guarantee an undisturbed transfer of the signal (van Ommen et al., 1999). A Kistler sensor, type 7261, was connected to this probe to measure the differential pressure fluctuations.

The pressure fluctuations in the rotating distributor bed ($D = 0.19$ m) were measured using 2 pressure probes (Fig. 1). The pressure probes were placed through the bed wall; one probe was placed at the plenum and the other was placed above the distributor at a height of $0.75D/2$. The probe dimensions for this facility are similar to those of the smaller facility. Two Kistler and Honeywell (SPT type) pressure sensors were placed in the plenum
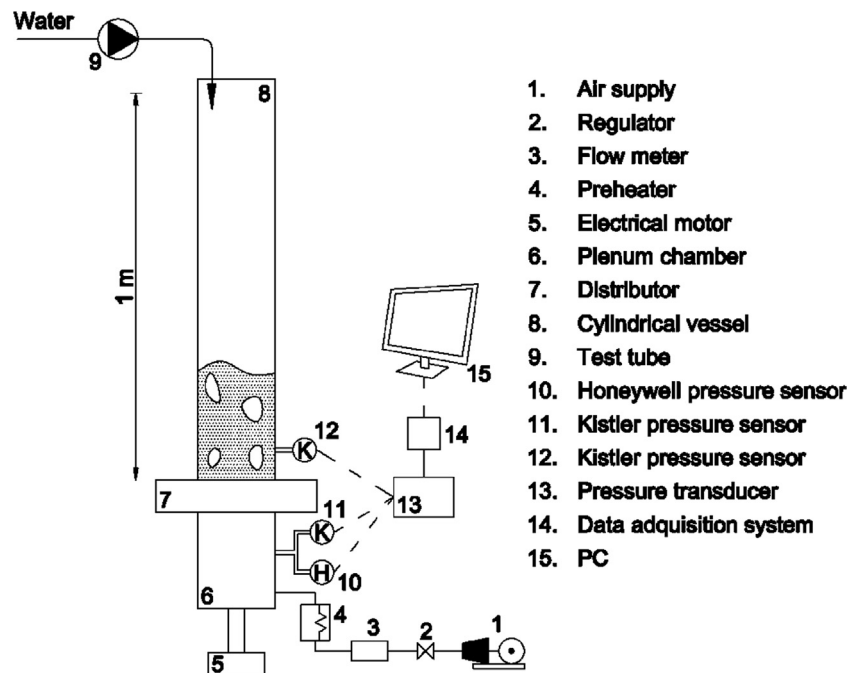


| | |
|---|---|
| 1. | Air supply |
| 2. | Regulator |
| 3. | Flow meter |
| 4. | Preheater |
| 5. | Electrical motor |
| 6. | Plenum chamber |
| 7. | Distributor |
| 8. | Cylindrical vessel |
| 9. | Test tube |
| 10. | Honeywell pressure sensor |
| 11. | Kistler pressure sensor |
| 12. | Kistler pressure sensor |
| 13. | Pressure transducer |
| 14. | Data adquisition system |
| 15. | PC |

**Fig. 1.** Schematic diagram of the experimental fluidized bed equipped with a rotating distributor.

chamber. Another Kistler sensor was placed at a height of $0.75D/2$ above the distributor.

The measurements from the Kistler sensors were amplified using a Kistler amplifier type 50515. The signals were stored on a PC using a National Instruments data acquisition system type 9234 for the Kistler measurements and type 9205 for the Honeywell pressure signals, working in both cases at a sampling frequency of 400 Hz. All signals were filtered through a low pass filter at 0.16 Hz and a high pass filter at 200 Hz.

## 3. Experimental procedure

To study the feasibility of the frequency division method, three types of tests were conducted (Table 1): (1) varying the relative fluidization velocity, $U_r = U/U_{mf}$, (2) changing the bed height, and (3) studying the water-induced defluidization process.

Experiments for the first type of test were conducted on the small fluidized bed ($d = 0.07$ m) by changing the relative velocity, $U_r$, from 1.9 to 3.78 at a constant bed aspect ratio of $h_b/d = 1$. The raw pressure signal data recorded at the plenum chamber with the Kistler sensor were used to determine the improvement of the proposed method compared with the visual detection method.

The well-known effect of the bed aspect ratio on the natural bed frequency was used to test the reliability of the frequency division method (van der Schaaf et al., 2004). By increasing the bed height of the fluidized bed equipped with the rotating distributor ($D = 0.19$ m), slug type fluidization was induced in the bed. The dynamic features of the fluidized bed were then modified by varying the bed aspect ratio, $h_b/D = 0.75, 1.5$ and $2$. In these tests, the relative fluidization velocity was constant at $U_r = 1.6$, where the bed was shown to be well-fluidized (Gómez-Hernández et al., 2012). The effect of the pressure probe location and the influence of the pressure sensor type were also analyzed.

Water-induced defluidization experiments were carried out using the rotating distributor facility ($D = 0.19$ m) to illustrate the use of the wide band energy as a monitoring tool. Applying the proposed frequency division methodology, the frequency domain was divided into three regions, in which the energy of the power spectrum was calculated. In these tests, the aspect ratio was fixed at $h_b/D = 0.75$, and the fluidization velocity was $U_r = 1.6$. According to Gómez-Hernández et al. (2012), the tests started with the bed working without the presence of agglomerates, i.e., nominal conditions. Then, 150 ml of water was injected on the surface of the bed, at a distance of 1 m perpendicular to the distributor, causing defluidization of the bed. The rotating distributor was then used to counteract the defluidization phenomenon.

## 4. Frequency division method

As stated above, the estimation of the wide band energy requires the identification of different frequency regions in the

**Table 1**
Summary of the experiments.

| Facility | Test | $h_b/D$ | $U_r$ | Distributor state |
|----------|------|---------|-------|-------------------|
| $d = 0.07$ m | 1 | 1 | 1.9 2.84 3.78 | – |
| $D = 0.19$ m | 2 | 0.75 1.5 2 | 1.6 | Static |
| | 3 | 0.75 | 1.6 | Static Rotating |

frequency domain. In this section, an unbiased and systematic method is proposed to identify the frequencies that divide the power spectrum.

The method assumes that the high energy region of the cumulative energy distribution can be approximated with a statistical distribution. The distribution fits the high energy region of the CE with high accuracy; this region is usually centered on the dominant frequency region of the spectrum. However, the CE distribution tails are not well-approximated by the statistical distribution. This result is used in the proposed method to identify the spectral boundary regions. The region of coincidence between the statistical and experimental CE distributions is identified using the Kolmogorov–Smirnov test. In this manner, the CE frequency distribution can be divided into three regions: Two poorly matched regions (Regions I and III), which correspond to the tails of the CE distribution, and a well-matched region (Region II), which corresponds to the highest energy content of the distribution. Several statistic distributions were analyzed to fit the cumulative energy distribution. The experimental conditions in this study favored the use of Student's $t$-distribution as the statistical distribution to fit the experimental data. The methodology can be applied using any statistical distribution that appropriately fits the data.

Student's $t$-distribution is well-known in statistics and, in its non-standardized form, is expressed as follows:

$$p(x|\mu, \lambda, \nu) = \frac{\Gamma(\nu+1/2)}{\Gamma(\nu/2)} \left(\frac{\lambda}{\pi\nu}\right)^{1/2} \left(1 + \frac{\lambda(x-\mu)^2}{\nu}\right)^{-(\nu+1)/2} \quad (1)$$

where $p(x)$ denotes the Student's probability density function (PDF) of the variable $x$ with location parameter $\mu$, scale parameter $\lambda > 0$, and shape parameter $\nu > 0$. These parameters are estimated according to the maximum-likelihood estimation (MLE) method (Dempster, 1977).

The Kolmogorov–Smirnov test is a simple method to test whether an empirical sample follows a specific distribution, which is the null hypothesis ($H_0$), against the alternative hypothesis ($H_1$) that it follows a different distribution. The test compares the empirical cumulative distribution function of the sample ($S_n(x)$) (i.e., the cumulative energy distribution), with the statistic cumulative distribution function (CDF), which is the fitted statistic distribution, Eq. (2), as follows:

$$D_n = \max|S_n(x) - CDF(x)| \quad (2)$$

where $D_n$ is the distance between the cumulative distributions. The distance, $D_n$, is used to obtain the modified statistic, $D^*$, as shown in Eq. (3), which will be compared to the critical values of the test for a certain level of significance, $\alpha$ (Stephens, 1970). The modified statistic, $D^*$, is a function of the sample size ($n$), computed as a function of the size of both cumulative distributions ($n_1$ and $n_2$) by Eq. (4) as follows:

$$D^* = D_n(\sqrt{n} + 0.11 + 0.12/\sqrt{n}) \quad (3)$$

$$n = \frac{n_1 n_2}{n_1 + n_2} \quad (4)$$

The Kolmogorov–Smirnov test is constructed by using the critical values of the Kolmogorov distribution (Stephens, 1970). The null hypothesis is rejected at level $\alpha$ if $D^* > K_\alpha$, where $K_\alpha$ is found from the Kolmogorov distribution as follows:

$$\Pr(K \leq K_\alpha) = 1 - \alpha \quad (5)$$

The procedure for processing the pressure data is outlined in Fig. 2 and can be summarized as follows:

- Determination of the power spectrum of the pressure signal using Welch's method (Welch, 1967).

- Computation of the cumulative energy in the frequency domain.
- Fitting of the cumulative energy function to the Student's $t$-distribution. The fitting was performed using the maximum-likelihood estimation method (MLE), assuming that the cumulative energy distribution is distributed as a Student's $t$-distribution with all unknown characteristic parameters (Dempster, 1977; Fisher, 1925).
- Determination of the goodness of fit between the cumulative energy and the Student's $t$-distribution's cumulative density (CDF) using the standard error of the estimated parameters. The standard errors of the location, scale and shape parameters were analyzed. It was found that when the standard error values of the shape parameter were below $\hat{\sigma}_\nu = 0.07$, the cumulative energy distribution was well-approximated by Student's $t$-distribution.
- Division of the frequency regions at the points where the cumulative density function of the Student's $t$-distribution ceased to satisfy the Kolmogorov–Smirnov test. The test distinguished between the tails of the energy distribution, which are not well-described by the Student's $t$-distribution, and the central frequency region which, in contrast, is well-approximated by the statistical distribution. The significance level presented a low influence on the cut-off frequencies, and for that reason, a typical value of $\alpha = 5\%$ was used in the Kolmogorov–Smirnov tests (Stephens, 1970).

To follow the procedure stated above, it is necessary to set some criteria for the number of samples ($N_s$) needed for the computation of each sub-spectrum using Welch's method. The procedure consists of the initial estimation of the PSD using $N_s = 1024$ samples for the computation of each sub-spectrum. Then, the CE is approximated by the Student's $t$-distribution CDF. The goodness of fit determines whether the frequency resolution is high enough to describe the characteristic frequencies of the system. If not, the number of points considered ($N_s$) is increased, and the procedure is restarted.

The effect of the number of samples on the standard error was investigated through examination of the data. The standard error of the power spectrum using $N_s = 4096$ was $\hat{\sigma}_\nu = 0.07$. If the number of samples was increased to $N_s = 8192$, the standard error decreased to $\hat{\sigma}_\nu = 0.049$. However, the decrease of the standard error caused a reduction of the frequency range where the Student's $t$-distribution matched the cumulative energy distribution; consequently, the central region of coincidence between both distributions decreased drastically. This decrease changed the energy distribution, leading to a possible failure of the Kolmogorov–Smirnov test when identifying the corresponding cut-off frequencies.

## 5. Results

The statistical frequency division method based on the Student's $t$-distribution approximation was applied to different measured pressure fluctuation signals collected either by Kistler or Honeywell pressure transducers. Several tests varying the relative gas velocity ($1.8 < U_r < 3.78$), performed in the small bed facility ($d = 0.07$ m), were analyzed to understand the operational limits of this method. The influence of the bed height on the Student's $t$-distribution fit and the measurement conditions were studied for the fluidized bed equipped with a rotating distributor ($D = 0.19$ m). Finally, water-induced defluidization tests are presented to illustrate the performance of the method as a monitoring tool (Table 1).

### 5.1. Dynamic aspects of the frequency division method: the gas velocity effect

Tests were conducted in the small bed facility to study the influence of the gas velocity on the frequency domain division. The proposed statistical method and the visual approach were applied and compared for different fluidization velocities ranging from $U_r = 1.9$ to 3.78 with constant $h_b/d = 1$.

The results of applying the statistical method to the pressure fluctuation signals are plotted in Fig. 3. In this figure, the degree of matching between the experimental results and the Student's $t$-distribution approach with both the power spectral density and the cumulative energy distribution is shown. Comparing these graphs, it can be appreciated that the determination of the good-ness of fit between both distributions is easier using the cumula-tive energy distributions. The change in the fluidization regime is detected by both the power spectrum and the cumulative energy distribution (Fig. 3). The results show that when the gas velocity was increased, a wider distribution of high energy frequencies was achieved. The Student's $t$-distribution CDF is close to the energy distribution in the range of frequencies where the sharp increase of energy appeared. This well-fitted Student's $t$-distribution region defines Region $t$-II, between the cut-off frequencies of the low ($f_{cI}$) and high ($f_{cII}$) frequency regions. According to these frequency limits (Fig. 3), the increase of the fluidization velocity produced a wider frequency range for Region $t$-II, covering most of the main characteristic frequencies shown in the spectrum, and therefore, showing sensitivity to bubbling dynamics. This result is a conse-quence of the wider range of frequencies with high energies, which can also be seen by comparing the $U_r = 1.9$ test (Fig. 3-a2) with the $U_r = 2.84$–3.78 tests (Fig. 3-b2/c2). Because the frequency boundaries of Region $t$-II are wider, the energy is mostly concen-trated in Region $t$-II and the energies of Regions $t$-I and $t$-III are relatively small (Table 2).
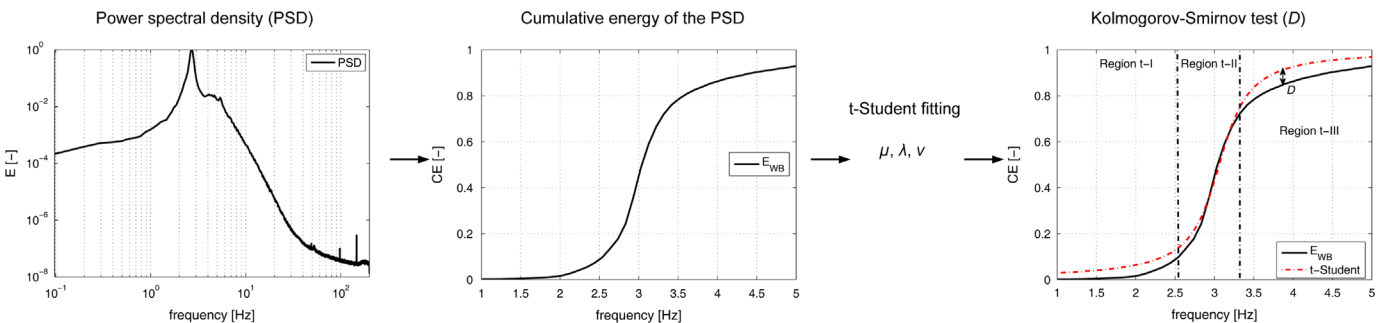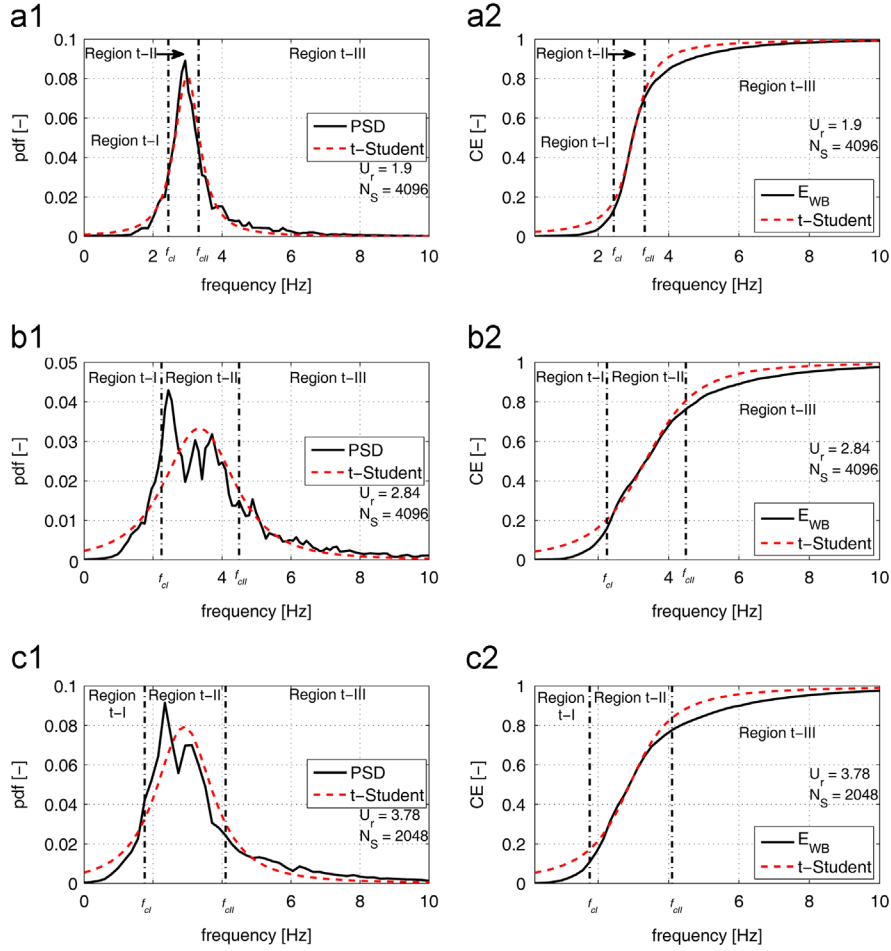


**Fig. 2.** Scheme of the frequency division method.

**Fig. 3.** Probability mass function and cumulative mass function for different fluidization velocities ($d=0.07$ m and $h_b/d=1$): (a1) PSD and (a2) CE for $U_r=1.9$, (b1) PSD and (b2) CE for $U_r=2.84$, (c1) PSD and (c2) CE for $U_r=3.78$.

**Table 2**
Effect of the velocity on the energy contained within the frequency regions of both methodologies.

| $U_r$ | Statistical approach [%] | | | Visual method [%] | | |
|---|---|---|---|---|---|---|
| | Region $t$-I ($\Delta f < f < f_{cI}$) | Region $t$-II ($f_{cI} < f < f_{cII}$) | Region $t$-III ($f_{cII} < f < f_N$) | Region 1 ($\Delta f < f < f_{cI}$) | Region 2 ($f_{cI} < f < f_{cII}$) | Region 3 ($f_{cII} < f < f_N$) |
| 1.9 | 10.10 | 60.33 | 29.57 | 83.22 | 16.68 | 0.10 |
| 2.84 | 13.04 | 63.23 | 23.73 | 88.80 | 11.12 | 0.08 |
| 3.78 | 6.65 | 70.97 | 22.38 | 89.45 | 10.22 | 0.33 |

The power spectra of the energy data for the three velocities are shown in logarithmic form in Fig. 4. According to this figure, the increase in gas velocity influenced the total power of the PSD function but minimally influenced its shape (van der Schaaf et al., 2004). The logarithmic representation allowed the visual identification of the frequency limits. Thus, applying the visual division approach, Region 1 presents the cut-off frequency at $f_{cI}=4$ Hz for $U_r=1.9$ and $f_{cI}=6$ Hz for $U_r=2.84$–3.78 tests. However, as these frequency limits were visually chosen, other boundary values could be selected in the 3.7–7 Hz frequency range with similar accuracy because it is not clear where the power (or exponential) fall-off with frequency begins (Johnsson et al., 2000). Similarly, it was difficult to find the upper frequency limit of Region 2 ($f_{cII}$). This frequency limit was fixed to $f_{cII}=23$ Hz for the $U_r=1.9$ and $f_{cII}=30$ Hz for the $U_r=2.84$–3.78 tests. The wide band energy values of the visual frequency regions were primarily found in Region 1 (Table 2). Those energy values were only slightly influenced by the lower frequency limit decrease, i.e., they merely increased because of the total power
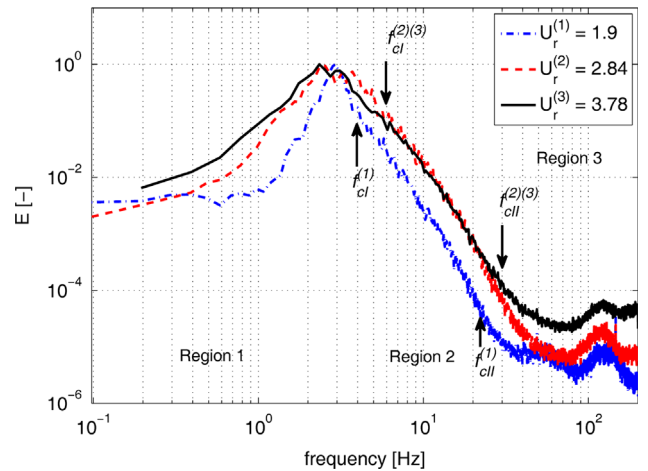


**Fig. 4.** Power spectrum for different fluidization velocities ($d=0.07$ m and $h_b/d=1$).

increase. In contrast, the energy of Region 3 was almost negligible and independent to changes in the fluidization velocity.

The comparison of these results showed that both methods detected changes in the fluidization velocity. However, in addition to the difficulties in selecting the cut-off frequencies, Region 3 can be neglected because it is nearly independent of changes in the fluidization velocity. In contrast, the three Student's $t$-distribution regions showed the effect of the gas velocity change.

### 5.2. Dynamic aspects of the frequency division method: the bed aspect ratio effect

It has been previously reported in the literature (Kage et al., 2000; van der Schaaf et al., 2004) that increasing the settled bed height at a constant gas velocity produces a decrease of the dominant frequency, while the power fall-off with frequency remains the same. This behavior is used to analyze both the sensitivity and reliability of the Student's $t$-distribution frequency division approach. The reliability is assessed by studying whether the proposed methodology can be applied using the plenum and bed Kistler pressure signals to: (i) divide the frequency domain, and (ii) detect the changes in the bed aspect ratio. Then, the results obtained with the Student's $t$-distribution methodology will be compared with the visual frequency division approach. To that end, tests were performed by changing the settled bed height, using values of $h_b/D = 0.75$, 1.5 and 2 at a constant air velocity ratio, $U_r = 1.6$, in the larger fluidized bed with a static distributor (Table 1).

The power spectra density functions and the cumulative energy distributions are shown in Fig. 5 for both pressure sensors. The results of the statistical methodology, i.e., the Student's $t$-distribution fitting and cut-off frequencies, are also plotted with the cumulative energy distributions (Fig. 5-a2/b2). As expected, similar power spectra and cumulative energy distributions are found for both pressure probes, a result found in previous work by Gómez-Hernández et al. (2012). Focusing on the pressure measurements at the plenum chamber (Fig. 5-a1/a2), the transition from shallow to deeper beds is shown by a decrease of the dominant frequencies and by the appearance of secondary frequency peaks.

The power spectra of Fig. 5-a1 shows that these dominant frequencies decrease from $f_c = 2.7$ Hz for the shallow bed to $f_c = 1.85$ and 1.41 Hz for $h_b/D = 1.5$ and 2, respectively. These characteristic frequencies are in accordance with those calculated with the equations proposed by Baskakov et al. (1986). The bed aspect ratio increase produced the appearance of some secondary peaks at approximately 2–4 Hz in the cases of $h_b/D = 1.5$ and 2, illustrating the slug like regime for the deepest bed. The bed height changes can also be detected using the cumulative energy distributions by the displacement of the abrupt energy increase to lower frequencies (Fig. 5-a2). The secondary peaks shown in the PSD (Fig. 5-a1) are also detected by the cumulative energy distribution (Fig. 5-a2) as a change in the slope at approximately 2–4 Hz. These secondary peaks shown in both the PSD and CE suggest the use of a bimodal distribution to describe the two modes shown in Fig. 5-a1 for the $h_b/D = 2$ test. This result indicates that the statistical distribution that fits the frequency domain depends on the experimental conditions. Nevertheless, the Student's $t$-distribution fitting of the $h_b/D = 2$ test also offered valuable results, and for that reason, only the approximation of that statistic distribution to the experimental results will be considered in this work. Similar results are obtained for the pressure probe inside the bed for the cut-off frequencies and energy content of the frequency regions, considering each aspect ratio separately. The results are shown in Table 3. There is only a noticeable difference between the frequency limits of the plenum and bed pressure probe for the $h_b/D = 0.75$ case.

Comparing the energy values of the beds with different aspect bed ratios, the results show that the energy contained in each region varies with the bed height change, as shown in Table 3.
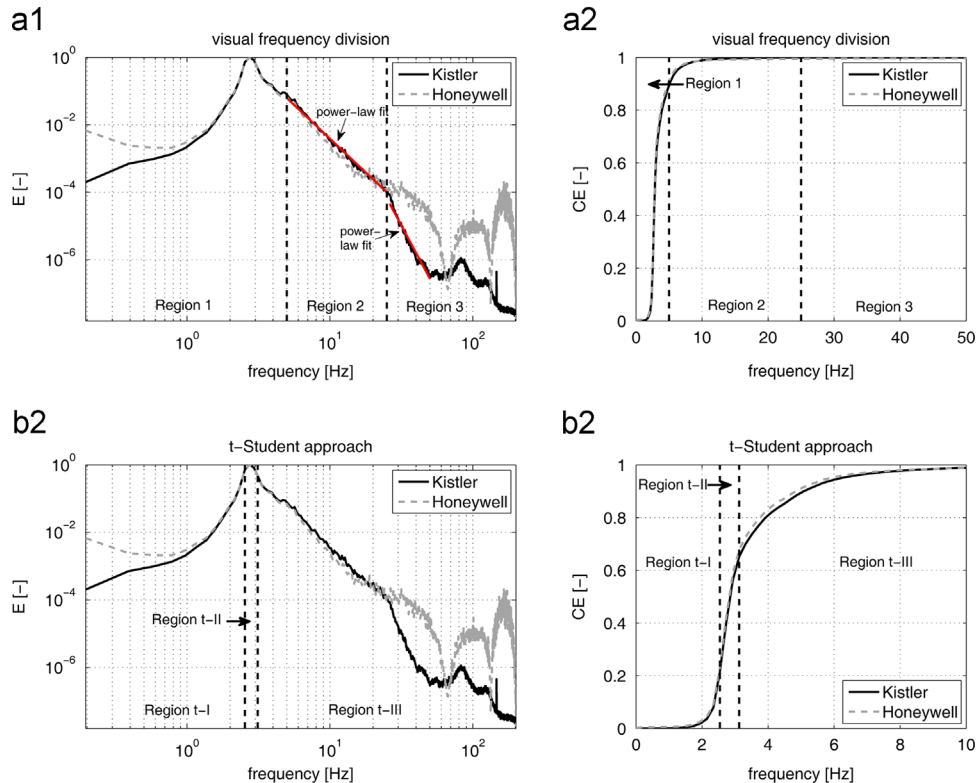


**Fig. 5.** The PSD and CE functions of a time series pressure signal with varying bed heights ($D = 0.19$ m and $U_r = 1.6$). (a1) PSD of the plenum sensor, (a2) CE of the plenum sensor, (b1) PSD of the bed sensor, (b2) CE of the bed sensor.

**Table 3**
Frequency division results for the bed equipped with a rotating distributor for different bed heights, Kistler sensors ($D=0.19$ m and $U_r=1.6$).

| $h_b/D$ | Pressure probe location | Cut-off frequencies [Hz] | | Mean energy content [%] | | |
| | | $f_{cI}$ | $f_{cII}$ | Region $t$-I ($\Delta f < f < f_{cI}$) | Region $t$-II ($f_{cI} < f < f_{cII}$) | Region $t$-III ($f_{cII} < f < f_N$) |
|---|---|---|---|---|---|---|
| 0.75 | Plenum | 2.54 | 3.32 | 7.35 | 58.32 | 34.33 |
| | $h=7$ cm | 2.05 | 3.51 | 9.00 | 65.66 | 25.34 |
| 1.5 | Plenum | 1.76 | 2.15 | 30.33 | 22.87 | 46.80 |
| | $h=7$ cm | 1.76 | 2.15 | 35.78 | 26.01 | 38.20 |
| 2 | Plenum | 1.95 | 2.25 | 56.58 | 8.91 | 34.51 |
| | $h=7$ cm | 1.95 | 2.15 | 58.71 | 5.64 | 35.65 |

**Table 4**
Frequency division from the visual inspection method, Kistler sensor placed at the plenum ($D=0.19$ m and $U_r=1.6$).

| $h_b/D$ | Cut-off frequencies [Hz] | | Mean energy content [%] | | |
| | $f_{cI}$ | $f_{cII}$ | Region 1 ($\Delta f < f < f_{cI}$) | Region 2 ($f_{cI} < f < f_{cII}$) | Region 3 ($f_{cII} < f < f_N$) |
|---|---|---|---|---|---|
| 0.75 | 5 | 25 | 89.3 | 10.67 | 0.03 |
| 1.5 | 4 | 20 | 91.11 | 8.88 | 0.01 |
| 2 | 3 | 20 | 85.91 | 14.08 | 0.01 |

The frequency peaks evident at frequencies higher than the dominant frequency for deep beds change the slope of the cumulative energy distribution; thus, the region of approximation between the Student's $t$-distribution and the cumulative energy distribution is different. Therefore, as the frequency limits change, the dynamic features and the physical meanings attributed to the different frequency regions also change with the bed aspect ratio. Similar to the results found from Fig. 4, for $h_b/D=0.75$ and 1.5 (Fig. 5), Region $t$-II is related to the bulk dynamics because it contains the dominant frequency of the bed, whereas Regions $t$-I and $t$-III represent the slow and the fast fluidization phenomena. However, the energy increase of the secondary frequency peaks shown in Fig. 5-a2 for the deepest bed ($h_b/D=2$) cause the Student's $t$-distribution fit to the cumulative energy distribution at higher frequencies, focusing Region $t$-II on these secondary peaks. Therefore, in this case, Region $t$-I now includes the main frequency of the bed, whereas Region $t$-II identifies the slug-like regime and Region $t$-III the fast fluidization phenomenon. From these results, it is concluded that as the bed height is increased, the energy of Region $t$-II diminishes, transferring a large portion of its energy to Region $t$-I, whereas the energy contained in the high frequency region (Region $t$-III) remains nearly constant.

Once the ability of the Student's $t$-distribution methodology to detect changes in the bed aspect ratio was verified, its perfor-mance was studied by comparing the results with the visual frequency division method. As stated previously, the cut-off fre-quencies were visually fixed according to the changes in the power fall-off with frequency. The frequency limits and the energy con-tained in each region is shown in Table 3. These results show that the frequency limits of Regions 1 and 2 ($f_{cI}$) decrease as the bed height is increased because the major frequency content of the pressure fluctuations move to lower frequencies (Kage et al., 2000). This type of frequency decrease did not appear for the cut-off frequencies in Regions 2 and 3 ($f_{cII}$). The energy computation within these frequency regions confirms that Region 3 is influenced neither by the fluidization nor by the bed height increase. The energy of all frequency regions remains nearly constant with the bed height increase. This is because Region 1 always contains nearly 90% of the spectral energy (Table 4). Therefore, regardless of the successful previous application of the visual inspection method for the char-acterization of the power spectrum (Johnsson et al., 2000; van der Schaaf et al., 1999; Vander Stappen, 1996), the corresponding wide band energy distribution detected no bed aspect ratio effect, and consequently, the subsequent monitoring performance would be less sensitive than that obtained by the wide band energy measured using the Student's $t$-distribution approach. As shown in Table 3, the proposed Student's $t$-distribution approach detected the bed height changes in a measurable way.

### 5.3. Pressure sensors rating effect

One of the primary drawbacks of the visual frequency division method is the bias caused by the observer when selecting the frequency limits. The measured pressure signal can be affected by noise, which hinders the detailed description of the high fre-quency spectral region. Moreover, pressure sensor rating and signal conditioning can affect the signal quality and therefore, the frequency limit identification. For instance, the power spec-trum fall-off, which is critical for using the visual inspection method, can be significantly different if an industrial or laboratory pressure sensor is used.

Therefore, the possible effect of the pressure sensor rating for both the visual and unbiased Student's $t$-distribution approaches was investigated. Pressure fluctuations recorded at the plenum chamber with both the Kistler and the Honeywell transducers were analyzed using both methods. The experimental runs were conducted in the 19-cm ID fluidized bed facility operating with the static distributor at $U_r=1.6$ for 4 min. The Honeywell transducers, widely used in industrial applications, are characterized by a high level of noise in the raw pressure fluctuation signal; thus, the signal must be filtered. The spurious crossings in the raw Honeywell data produced aliasing problems leading to incorrect power spectrum estimation at high frequencies. Honeywell pressure-time signals were filtered using a moving average filter. A finite impulse filter (FIR) attenuates the high frequencies while retaining a sharp step response. The averaging window length of the filter was set according to the average cycle time of the unfiltered pressure signal (vander Stappen, 1996). In contrast to the Honeywell measurements, the high quality of the Kistler pressure signals ensured correct power spectrum estimation from the raw pressure data.

Fig. 6 shows the frequency regions obtained using both methods from the Kistler and Honeywell pressure signals. The corresponding power spectra (Fig. 6-a1/b1) and cumulative energy distributions (Fig. 6-a2/a2) were estimated for the measured Kistler signals (raw data) and for the filtered Honeywell data. The results from the visual inspection method (Region 1, 2 and 3) are presented in Fig. 6-a1/a2, and the Student's $t$-distribution frequency regions (Region $t$-I, $t$-II and $t$-III) are shown in Fig. 6-b1/b2.

As stated previously, the visual frequency division starts with the power spectrum estimation and the evaluation of the power decay with frequency. As the results show for the Kistler PSD (Fig. 6-a1), there is a sharp frequency peak at $f_c=2.734$ Hz in the power spectrum, which is followed by two different power fall-off regions with frequencies that can be fitted with similar accuracy either to exponential, $P_{xx} \sim \exp(-f/\mu)$, or power functions, $P_{xx} \sim f^{-\alpha}$ (Johnsson et al., 2000; van der Schaaf et al., 1999). The visual inspection of Fig. 6-a1 suggests that the frequency domain can be divided into three regions because the power fall-off with fre-quency changes at approximately 3 to 6 Hz and 20 to 30 Hz. The cut-off frequency between Regions 1 and 2 was placed at $f_{cI}=5$ Hz, and the frequency limit between Regions 2 and 3 is visually
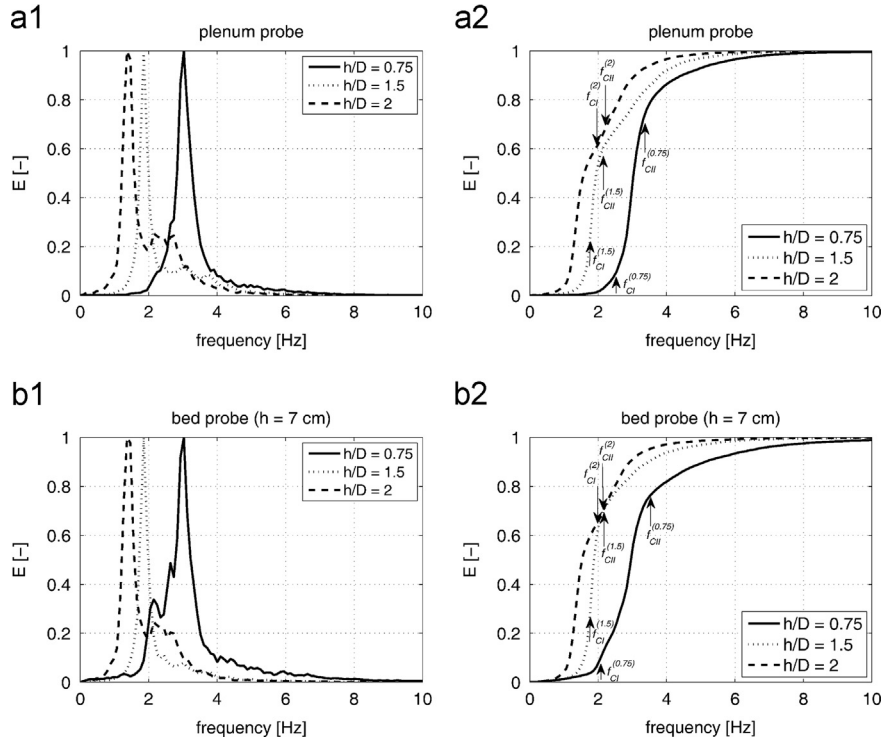
**Fig. 6.** Frequency regions from the PSD of the Kistler and Honeywell pressure sensors placed at the plenum ($N_s=2048$, $D=0.19$ m, $h_b/D=0.75$ and $U_r=1.6$): (a1) power spectra and (a2) cumulative energy distributions of the visual inspection approach; (b1) power spectra and (b2) cumulative energy distributions of the Student's $t$-distribution approach.

selected to be $f_{cII}=25$ Hz. Similar results are shown for the Honeywell pressure signal up to $f_{cII}=25$ Hz. At 25 Hz, the Honeywell power spectrum experiences a high level of noise, which prevents the development of the power-law fitting of Region 3 and the rigorous application of the visual inspection method.

In spite of the differences at the higher frequencies of the spectra (Region 3), both the Kistler and Honeywell spectral domains can be visually divided with the same frequency limits; consequently, the frequency regions represent identical fluidization processes. These frequency regions are also plotted in energy terms with the cumulative energy distributions for both pressure sensors in Fig. 6-a2. The results in this figure show no significant differences between the two cumulative energy distributions because most of the characteristic frequencies of the bed are contained in Region 1 and Region 2, where the signal noise is negligible. Regarding the spectral regions resulting from the Student's $t$-distribution approach, no meaningful differences can be observed either in the PSD (Fig. 6-b1) or in the cumulative energy distribution (Fig. 6-b2) between the Kistler and Honeywell data. Therefore, from the point of view of the pressure sensor rating, both the visual inspection method and the Student's $t$-distribution approach are unaffected because the influence of the noise is restricted to Region $t$-III.

However, the sizes of the resulting regions are different, depending on which method is used to find the boundaries of the three regions. Therefore, the characteristic frequencies are likely to produce a different sensitivity in the wide-band energy calculated from the visual inspection and the Student's $t$-distribution methods. To understand the response of the wide band energy to dynamic changes in the fluidized bed, their dynamic responses are compared.

Regarding the visual inspection method, Region 1 represents the macro-structure of the flow because it contains most of the characteristic frequencies of the bed dynamics (Johnsson et al., 2000; van der Schaaf et al., 1999). However, only limited

information about the nature of the macro-structure dynamics in the fluidized bed has been reported in the literature. Therefore, it is difficult to assign relative weights to the different bed dynamic scales in Region 1 for the fluidization conditions caused by the multiscale features of the bed dynamics. Nevertheless, the description serves to explain the wide band energy behavior from a monitoring point of view. As a result of the presence of the high power frequency peaks within Region 1 (Fig. 6-a1), $E_{WB1}=89\%$ of the spectral energy is concentrated in Region 1. In contrast, Region 2 represents nearly $E_{WB2}=10\%$ of the spectral energy and includes the inflection points that appeared in the cumulative energy distributions as a result of the abrupt energy change following the dominant frequency. Traditionally, Region 2 has been related to the finer structures of the bed (fast dynamic processes) (Johnsson et al., 2000; van der Schaaf et al., 1999). Finally, the high frequency region involves less than $E_{WB3}=1\%$ of the energy, proving that Region 3 has no clear dependence on the fluidization regime (Briongos and Guardiola, 2003; Johnsson et al., 2000).

Different frequency regions were obtained applying the Student's $t$-distribution approach, illustrated by comparing Fig. 6-a1/a2 with Fig. 6-b1/b2. The proposed statistical method disregards the previous physical interpretation of the spectrum and centers the division of the frequency domain on the mean frequency value. According to this approach, the region of coincidence between the Student's $t$-distribution and the cumulative energy distribution defines Region $t$-II. Fig. 6-b2 shows the results of applying this method to the cumulative energy distributions obtained with the Kistler and Honeywell sensors. The frequency limits were fixed at $f_{cI}=2.5$ Hz and $f_{cII}=3.1$ Hz dividing the frequency domain into the lower (Region $t$-I) and upper (Region $t$-III) tails of the cumulative energy distribution that were a worse approximation of the data by the Student's $t$-distribution function. As shown in Fig. 6-b1, for this case, the frequency limits divided the frequency spectra around the dominant frequency of the bed. The energy is now primarily

focused in Region $t$-II ($E_{WBII}$=59%), whereas $E_{WBI}$=7% and $E_{WBIII}$=34% of the energy are distributed in Regions $t$-I and $t$-III, respectively. Because of the difference in the cut-off frequencies and in the region size, the energy values and the dynamic processes related to each region are also different. Nevertheless, similar to the visual inspection method, the physical phenomena that characterize the spectra of Fig. 6-b1/b2, which correspond to the Student's $t$-distribution approach, can be identified in terms of the time scale dynamics as follows:

– Region $t$-I ($\Delta f < f < 2.5$ Hz) represents the larger structures of the bed which are governing the low frequency dynamics and consequently drive the long-term dynamics of the bed.
– Region $t$-II (2.5 Hz $< f < 3.1$ Hz) contains the dominant/mean frequency of the bed, suggesting that it is related to the bulk dynamics of the bed.
– Region $t$-III (3.1 Hz $< f < f_N$) includes the high frequency region of the spectrum and is related to the fast fluidization phenomena.
– The results in Fig. 6 show that the different energy contents resulting from the visual inspection and Student's $t$-distribution method are caused by different distributions of the characteristic frequencies. In the case of the visual frequency division, there is a region that contains almost all the characteristic frequencies (Region 1) and high frequency regions that represent the fast

fluidization phenomena (Region 2 and 3). However, for the Student's $t$-distribution approach, the location of the cut-off frequencies around the dominant frequency allowed the division of the macro-structure of the flow, and consequently, the division of the previous Region 1 into several sections. This division can be illustrated by comparing the frequency limits of Region 1 ($\Delta f < f < 5$ Hz), Region 2 (5 Hz $< f < 25$ Hz) and Region 3 (25 Hz $< f$), with the cut-off frequencies of Regions $t$-I ($\Delta f < f < 2.5$ Hz), $t$-II (2.5 Hz $< f < 3.1$ Hz) and Region $t$-III (3.1 Hz $< f < f_N$). The new division of the bed frequencies provides a better sensitivity of the wide band energy parameter for describing bubbling dynamics.

### 5.4. Application to detection of the defluidization phenomena

Water-induced agglomeration tests were performed to illustrate the use of the wide band energy as a monitoring tool. These tests were conducted to reduce the fluidization quality through the defluidization of the bed and the subsequent recuperation processes. Thus, the wide band energy was estimated using the frequency regions obtained with the Student's $t$-distribution (Fig. 7) and visual inspection (Fig. 8) methods. The cut-off frequencies were previously detailed in Fig. 6-b1/b2, for the
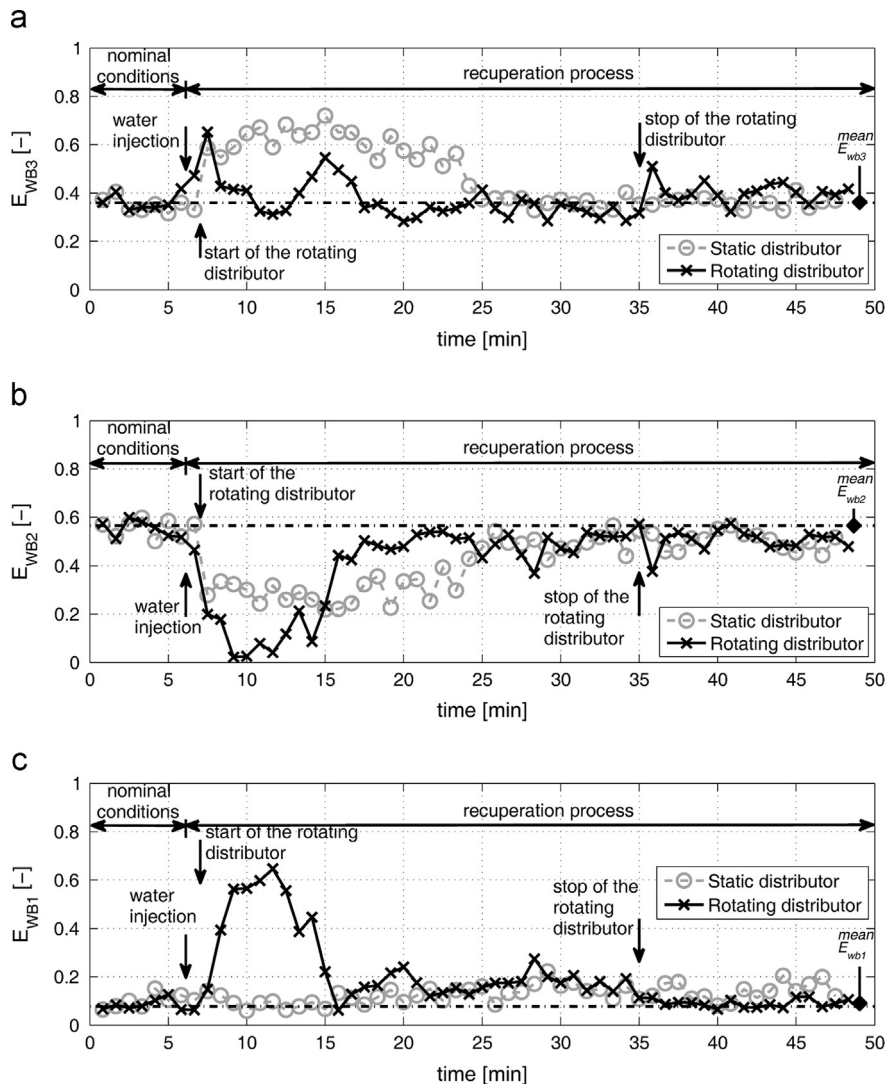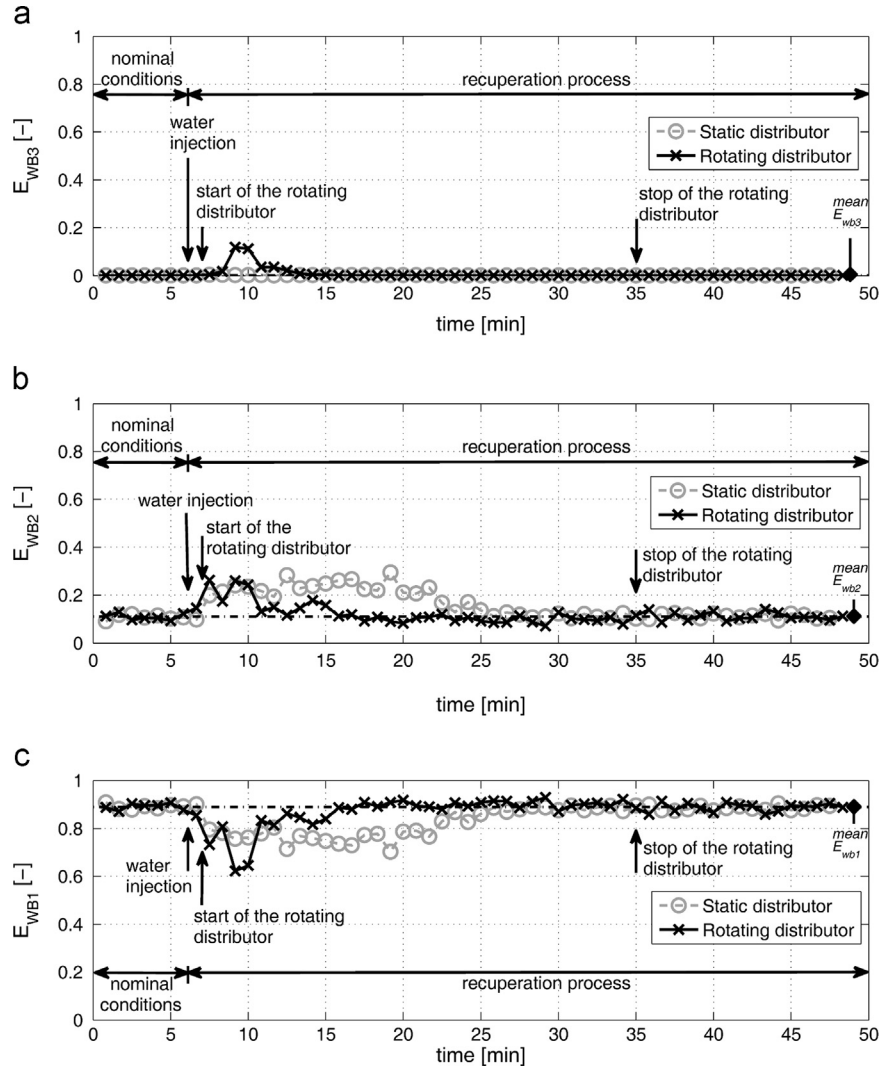


**Fig. 7.** Wide band energy measured in the Student's $t$-distribution regions for the Kistler sensor. (a) Region $t$-III (3.12 Hz $< f < f_N$). (b) Region $t$-II (2.54 Hz $< f < 3.12$ Hz Hz). (c) Region $t$-I ($\Delta f < f < 2.54$ Hz).

**Fig. 8.** Wide-band energy measured in the visual frequency regions for the Kistler sensor. (a) Region 3 ($25\,\text{Hz} < f < f_N$). (b) Region 2 ($5\,\text{Hz} < f < 25\,\text{Hz}$). (c) Region 1 ($\Delta f < f < 5\,\text{Hz}$).

Student's $t$-distribution, and in Fig. 6–a1/a2, for the visual method. The wide band energy for the pressure signals was estimated every 50 s throughout the entire test.

The agglomeration tests were conducted in the fluidized bed equipped with a rotating distributor ($D=0.19$ m) analyzing the Kistler signals recorded at the plenum chamber. The runs started with the bed working at $U_r=1.6$ and $h_b/D=0.75$ using the static distributor; these conditions are referred to as nominal conditions. After 6 min, 150 ml of water was injected onto the bed surface, causing the defluidization of the bed (Gómez-Hernández et al., 2012). Then, two different attempts to recover fluidization quality were performed: (1) with the static distributor and (2) with the rotating distributor.

The wide band energy values obtained using the Student's $t$-distribution frequency regions are shown in Fig. 7. In this figure, the three control charts correspond to the three frequency regions into which the frequency domain was divided. On each chart, the wide band energy values are shown with a black line for the rotating distributor, and with a gray line for the static distributor recuperation. The mean value of the wide band energy at nominal conditions is shown as a reference value.

The water injection formed sticky agglomerates on the bed surface that tended to settle on the top of the distributor. This growth of dead zones over the distributor caused the defluidization of the bed and the appearance of channels near the injection zone, which modified the air distribution in the bed. This bed defluidization was detected by the wide band energy of Regions $t$-II and $t$-III (Fig. 7-a/b). As shown in Fig. 7, the punctual injection of water produced a substantial energy transfer of 20% from Region $t$-II (Fig. 7-b) to the higher frequencies in Region $t$-III (Fig. 7-a), caused by the appearance of channels around the injection zone. This energy transfer to the higher frequencies confirms that Region $t$-III is related to the fast phenomena. Further-more, the energy loss in Region $t$-II indicates that the bulk movement of the bed was hindered by the agglomeration formation, suggesting the defluidization of the bed. In contrast, the energy of Region I is not affected by the water injection, as shown during the static distributor recuperation process in Fig. 7-c, suggesting that the larger structures of the flow field, such as the bubble pattern, remain unaffected during the agglomerate formation. Visual observation of the tests showed that the agglomerates were not homogenously distributed within the bed, allowing the presence of a bubbling zone opposite the injection zone. This phenomenon explains why the wide-band energy of Region $t$-I was not affected by the water injection: a bubbling zone was maintained within the bed that preserved the long term behavior of the pressure measurements.

The recuperation process with the static distributor was only affected by the air flow; consequently, the agglomerate breakage was a slow phenomenon, requiring 19 min to return to the

nominal conditions, as shown for Regions $t$-II and $t$-III (Fig. 7-a/b). Because of the slow rate of agglomerate destruction, there were channels during most of the recuperation process with the static distributor. In contrast, the rotating distributor reached nominal conditions for the mean wide band energy values 10 min after the water injection. The start of the distributor rotation produced an effect in the entire frequency domain, according to the Student's $t$-distribution frequency regions (Fig. 7). The homogeneous bubble distribution caused by the distributor rotation at 100 rpm imposed a local structure on the bed dynamics (Gómez-Hernández et al., 2012). Moreover, the rotating effect broke the dead zones between the holes of the distributor, where the agglomerates were settled, and thus improving the channel destruction. The data for Region $t$-III in Fig. 7-a show that 1 min after the start of the distributor rotation, almost all channels had disappeared. This effect was detected immediately after switching on the distribution rotation, when the three energy regions suddenly changed their energy values, transferring almost 30% of the energy from Region $t$-III to Region $t$-I, as shown in Fig. 7-a/c. However, the agglomerates detached from the water injection zone were distributed on the fluidized bed as a consequence of the distributor rotation, reducing the fluidization quality for a few moments. That process is reflected by the energy transference from Region $t$-II to Region $t$-I (Fig. 7-b/c), pointing out that there is a change in the bed structure after the start of the distributor rotation.

Fig. 8 shows the wide band energy results using the visual frequency regions. As stated above, the frequency regions obtained with the visual approach are related to different phenomena than the Student's $t$-distribution regions. In the case of the visual inspection method, Region 1 contains all the high frequency peaks and it is related to the macro-structure of the flow, whereas Regions 2 and 3 represent the finer structures. Therefore, the wide band energy of these frequency regions (Fig. 8) shows that the energy is primarily focused in Regions 1 ($E_{WB1} = 90\%$) and 2 ($E_{WB2} = 10\%$), whereas the energy value of Region 3 is insignificant in contrast to the Student's $t$-distribution results (Fig. 7). The data shown in Fig. 8-b/c show that the water injection is detected by a 10% energy transference between Regions 1 and 2. The energy increase of the high frequencies (Region 2) highlights the channel formation. However, Region 3 is barely affected by the water injection (Fig. 8-a). In spite of that, according to Regions 1 and 2 (Fig. 8-b/c) 19 min were needed to recover the fluidization quality with the static distributor test, which is close to the time obtained by the Student's $t$-distribution frequency regions (Fig. 8).

The effect of starting the distributor rotation is shown by the energy transferred from the higher (Region 2) to the lower (Region 1) frequencies due to the destruction of the channels (Fig. 8-b/c). According to the data, the distributor rotation only needed 5 min to recover the fluidization state and return to the nominal conditions. In contrast, the visual inspection during the test and the previous results showed that the recuperation process required at least 10 min to recover the initial fluidization quality. The false alarm can be explained by the wide frequency limits of Region 1. The start of the rotating distributor and the change in the fluidization pattern were codified at the lower frequencies (Region $t$-I). Because Region 1 contains all the frequencies up to $f_{cl} = 4$ Hz, the energy increase produced by the start of the rotating distributor shown in Region $t$-I ($\Delta f < f < 2.54$ Hz) directly supports the wide band energy of Region 1 ($\Delta f < f < 4$ Hz). The appearance of a false alarm proves that the frequency limits of Region 1 are too wide to discriminate between the larger structures and the macro-structure of the flow field. Therefore, in spite of the detection of the channel destruction from the start of the distributor rotation (shown in Region 2, Fig. 8-b), the frequency regions obtained through the visual approach were not able to monitor the agglomeration tests.

## 6. Conclusions

The methodology proposed for the unbiased and systematical frequency domain division using the Student's $t$-distribution approximation of the cumulative energy distribution improved the sensitivity of the wide band energy analysis. This method fixed the number of samples needed to estimate the power spectra, and the corresponding cumulative energy distribution, using the Kolmogorov–Smirnov test. The reliability of the method to divide the frequency domain was shown for different fluidization velocities, changing the bed aspect ratio and using different pressure probes.

The comparison between the visual frequency division approach and the proposed methodology showed significant differences in the cut-off frequencies. The estimated wide band energy in the frequency regions obtained using the visual method was not able to detect changes in the bed aspect ratio or the start of the rotating distributor. In contrast, the sensitivity demonstrated by the statistical frequency division approach would enable wide band energy to be used as a diagnostic tool in fluidized bed processes.

The application of the proposed methodology showed that the frequency limits vary as a function of the fluidization conditions. The fluidization conditions can also change the physical meaning of the frequency regions. The description of the physical meaning can be related to the time scales, and thus the different fluidization phenomena can be related to the wide band energy regions. This feature showed the capability of unbiased frequency regions to be used as a monitoring tool for water-induced defluidization tests, allowing the detection of some dynamic phenomena, such as channel formation, defluidization of the bed, and the start of the rotating distributor.

## Nomenclature

| | |
|---|---|
| $d$ | inner diameter of small fluidized bed vessel |
| $D$ | inner diameter of big fluidized bed vessel |
| $D_n$ | distance between cumulative distributions |
| $D^*$ | modified statistic of the Kolmogorov–Smirnov test |
| $E_{WB}$ | wide band energy |
| $f$ | frequency |
| $f_c$ | characteristic frequency |
| $f_{cI}$ | lower cut-off frequency |
| $f_{cII}$ | upper cut-off frequency |
| $f_N$ | Nyquist frequency |
| $\Delta f$ | frequency resolution |
| $h_b$ | fixed bed height |
| $H_0$ | null hypothesis |
| $H_1$ | alternative hypothesis |
| $K_\alpha$ | Kolmogorov threshold value |
| $n$ | sample size |
| $N_S$ | number of samples |
| $p(x)$ | probability of $x$ |
| $S_n(x)$ | empirical cumulative distribution of $x$ |
| $U_r$ | relative gas velocity |
| $U_{mf,r}$ | minimum fluidization velocity with rotating distributor |
| $U_{mf,s}$ | minimum fluidization velocity with static distributor |

*Greek symbols*

| | |
|---|---|
| $\alpha$ | significance level |
| $\lambda$ | scale parameter |
| $\mu$ | location parameter |
| $\nu$ | shape parameter |
| $\hat{\sigma}$ | standard error |

## Abbreviations

| | |
|---|---|
| BFB | bubbling fluidized beds |
| CDF | cumulative density function |
| CE | cumulative energy |
| MLE | maximum-likelihood estimation method |
| PMMA | poly methyl methacrylate |
| PSD | power spectral density |

## Acknowledgments

## References

Baskakov, A.P., Tuponogov, V.G., Filippovsky, N.F., 1986. A Study of Pressure-Fluctuations in a Bubbling Fluidized-Bed. Powder Technol. 45 (2), 113–117.

Briongos, J.V., Guardiola Soler, J., 2003. Free top fluidized bed surface fluctuations as a source of hydrodynamic data. Powder Technol. 134 (1–2), 133–144.

Brown, R.C., Brue, E., 2001. Resolving dynamical features of fluidized beds from pressure fluctuations. Powder Technol. 119, 2–3.

Chilekar, V.P., Warnier, M.J.F., van der Schaaf, J., Kuster, B.F.M., Schouten, J.C., van Ommen, J.R., 2005. Bubble size estimation in slurry bubble columns from pressure fluctuations. AIChE J. 51 (7), 1924–1937.

de Martin, L., van den Dries, K., van Ommen, J.R., 2011. Comparison of three different methodologies of pressure signal processing to monitor fluidized-bed dryers/granulators. Chem. Eng. J. 172, 1.

Dempster, A., 1977. Maximum likelihood from incomplete data via EM algorithm. J. R. Stat. Soc. Ser. B, Methodological 39 (1), 1–38.

Fisher, R.A., 1925. Theory of statistical estimation. Math. Proc. Cambridge Philos. Soc. 22 (05), 700.

Geldart, D., 1973. Types of gas fluidization. Powder Technol. 7 (5), 285–292.

Gómez-Hernández, J., Soria-Verdugo, A., Briongos, J.V., Santana, D., 2012. Fluidized bed with a rotating distributor operated under defluidization conditions. Chem. Eng. J. 195–196 (0), 198–207.

Johnsson, F., Zijerveld, R.C., Schouten, J.C., van den Bleek, C.M., Leckner, B., 2000. Characterization of fluidization regimes by time-series analysis of pressure fluctuations. Int. J. Multiphase Flow 26 (4), 663–715.

Kage, H., Agari, M., Ogura, H., Matsuno, Y., 2000. Frequency analysis of pressure fluctuation in fluidized bed plenum and its confidence limit for detection of various modes of fluidization. Adv. Powder Technol. 11 (4), 459–475.

Parise, M.R., Silva, C.A.M., Ramazini, M.J., Taranto, O.P., 2011. Identification of defluidization in fluidized bed coating using the Gaussian spectral pressure distribution. Powder Technol. 206 (1–2), 149–153.

Ruthiya, K.C., Chilekar, V.P., Warnier, M.J.F., van der Schaaf, J., Kuster, B.F.M., Schouten, J.C., van Ommen, J.R., 2005. Detecting regime transitions in slurry bubble columns using pressure time series. AIChE J. 51 (7), 1951–1965.

Sobrino, C., Almendros-Ibanez, J.A., Santana, D., De Vega, M., 2008. Fluidization of Group B particles with a rotating distributor. Powder Technol. 181 (3), 273–280.

Soria-Verdugo, A., Garcia-Hernando, N., Almendros-Ibanez, J.A., Ruiz-Rivas, U., 2011. Motion of a large object in a bubbling fluidized bed with a rotating distributor. Chem. Eng. Process. 50 (8), 859–868.

Stephens, M.A., 1970. Use of Kolmogorov–Smirnov, cramer–Von mises and related statistics without expensive tables. J. R. Stat. Soc. Ser. B-Stat. Methodol. 32 (1), 115–122.

van der Schaaf, J., Schouten, J.C., van den Bleek, C.M., 1998. Origin, propagation and attenuation of pressure waves in gas–solid fluidized beds. Powder Technol. 95, 220–233.

van der Schaaf, J., Johnsson, F., Schouten, J.C., van den Bleek, C.M., 1999. Fourier analysis of nonlinear pressure fluctuations in gas-solids flow in CFB risers - Observing solids structures and gas/particle turbulence. Chem. Eng. Sci. 54 (22), 5541–5546.

van der Schaaf, J., Schouten, J.C., Johnsson, F., van den Bleek, C.M., 2002. Non-intrusive determination of bubble and slug length scales in fluidized beds by decomposition of the power spectral density of pressure time series. Int. J. Multiphase Flow 28 (5), 865–880.

van der Schaaf, J., van Ommen, J.R., Takens, F., Schouten, J.C., van den Bleek, C.M., 2004. Similarity between chaos analysis and frequency analysis of pressure fluctuations in fluidized beds. Chem. Eng. Sci. 59 (8–9), 1829–1840.

van Ommen, J.R., Schouten, J.C., vander Stappen, M.L.M., van den Bleek, C.M., 1999. Response characteristics of probe-transducer systems for pressure measurements in gas-solid fluidized beds: how to prevent pitfalls in dynamic pressure measurements. Powder Technol. 106 (3), 199–218.

van Ommen, J.R., Sasic, S., van der Schaaf, J., Gheorghiu, S., Johnsson, F., Coppens, M., 2011. Time-series analysis of pressure fluctuations in gas-solid fluidized beds–A review. Int. J. Multiphase Flow 37 (5), 403–428.

vander Stappen, M. L. M., 1996. Chaotic Hydrodynamics of Fluidized Beds. (Ph.D. thesis), Delftt University of Technology.

Welch, P., 1967. The use of fast Fourier transform for the estimation of power spectra: a method based on time averaging over short, modified periodograms. IEEE Tran. Audio Electroacoust. 15 (2), 70.